Nuclear Instruments and Methods in Physics Research A 806 (2016) 109–116

Contents lists available at ScienceDirect

Nuclear Instruments and Methods in Physics Research A

journal homepage: www.elsevier.com/locate/nima

Accelerated radiation damage test facility using a 5 MV tandem ion accelerator

P.T. Wady [a,*], A. Draude [a], S.M. Shubeita [a], A.D. Smith [a], N. Mason [a], S.M. Pimblott [a,b], E. Jimenez-Melero [a,c]

[a] Dalton Cumbrian Facility, University of Manchester, Westlakes Science & Technology Park, Moor Row, Cumbria CA24 3HA, UK
[b] School of Chemistry, University of Manchester, Oxford Road, Manchester M13 9PL, UK
[c] School of Materials, University of Manchester, Oxford Road, Manchester M13 9PL, UK

ARTICLE INFO

Article history:
Received 13 July 2015
Received in revised form
22 September 2015
Accepted 26 September 2015
Available online 11 October 2015

Keywords:
Radiation damage
Nuclear reactor materials
Ion accelerator
Ion–solid interactions
Gamma spectrometry

ABSTRACT

We have developed a new irradiation facility that allows to perform accelerated damage tests of nuclear reactor materials at temperatures up to 400 °C using the intense proton (<100 μA) and heavy ion (≈ 10 μA) beams produced by a 5 MV tandem ion accelerator. The dedicated beam line for radiation damage studies comprises: (1) beam diagnosis and focusing optical components, (2) a scanning and slit system that allows uniform irradiation of a sample area of 0.5–6 cm^2, and (3) a sample stage designed to be able to monitor in-situ the sample temperature, current deposited on the sample, and the gamma spectrum of potential radio-active nuclides produced during the sample irradiation. The beam line capabilities have been tested by irradiating a 20Cr–25Ni–Nb stabilised stainless steel with a 3 MeV proton beam to a dose level of 3 dpa. The irradiation temperature was 356 °C, with a maximum range in temperature values of ± 6 °C within the first 24 h of continuous irradiation. The sample stage is connected to ground through an electrometer to measure accurately the charge deposited on the sample. The charge can be integrated in hardware during irradiation, and this methodology removes uncertainties due to fluctuations in beam current. The measured gamma spectrum allowed the identification of the main radioactive nuclides produced during the proton bombardment from the lifetimes and gamma emissions. This dedicated radiation damage beam line is hosted by the Dalton Cumbrian Facility of the University of Manchester.

1. Introduction

Structural materials used for in-core fission reactor components face the challenge of maintaining their internal structure and integrity during their expected lifetime under extremely demanding conditions of elevated temperatures, intense radiation fields, high stress levels and aggressive coolants [1]. The potential life extension of the current nuclear reactor fleet or the realization of advanced fission and fusion reactors concepts [2–4] will require those materials to remain stable at even higher operating temperatures (<1000 °C) undergoing radiation damage levels above 50 displacements per atom (dpa) in the presence of alternative coolants (e.g. molten salts or liquid metals), and witnessing an increased production of hydrogen and helium (one to several hundreds of appm/dpa). This can potentially cause complex structural phenomena, such as irradiation creep, void swelling, phase instabilities or enhanced high-temperature helium embrittlement [5–7]. The occurrence of any of these radiation-induced structural phenomena and their effect on the material's properties should be predicted reliably, and consequently implemented into reactor design codes and assessment procedures for lifetime extensions [8,9].

In order to reach the sufficient level of reliability in our mechanistic understanding of radiation-induced structural processes in in-core reactor materials, we would need to accumulate relevant experimental data based on material tests under equivalent service conditions. Ideally we would aim to perform those tests using test reactors that would provide a similar neutron flux and energy spectrum. Unfortunately, access to those test reactors is limited, the feasible experiments would be lengthy and would yield highly active samples, whose post facto structural and mechanical characterization would require the use of specialised equipment in active labs. The possibility of using ion accelerators to simulate neutron damage emerged in the 1960s to study the potential changes in structure and properties of structural materials used in light water reactors [10]. The use of charged particles

* Corresponding author. Tel.: +44 1946 508888.
E-mail address: paul.wady@manchester.ac.uk (P.T. Wady).

http://dx.doi.org/10.1016/j.nima.2015.09.088

as a surrogate for neutron damage opens the door to perform accelerated studies of radiation damage in reactor-relevant materials with systematic variations of experimental conditions and reduced levels of sample activation [11,12]. This approach has recently been validated by comparing the radiation-induced defect structures in a ferritic/martensitic steel generated by heavy ions and neutrons [13], and also by assessing the irradiation assisted stress corrosion cracking behaviour in proton- and neutron-irradiated stainless steels [14]. Standard practices of using ion beams to emulate neutron damage have also been developed by the international community [15].

In this paper, we report the development of a new experimental facility to perform accelerated radiation damage experiments using the 5 MV tandem ion accelerator installed at the Dalton Cumbrian Facility (DCF) of The University of Manchester. DCF is accessible to potential users via the UK National Nuclear Users Facility network (www.nnuf.ac.uk). This facility allows systematic radiation damage studies of structural materials at controlled conditions of temperature, total dose and dose rate, using an intense beam of either light ions (H, He) or a range of heavy ions. We describe briefly the main accelerator and beam line components that yield a well-defined ion beam at the sample position, and afterwards we provide detailed information about the end station development, and how we measure the sample temperature, total charge deposited on the sample and potential activation levels using on-line gamma spectrometry. The capabilities of this irradiation facility have been tested by irradiating 20Cr–25Ni–Nb stabilised stainless steel, namely 20/25 stainless steel, used in UK Advanced Gas Reactor claddings [16] up to 3 dpa with a 3 MeV proton beam. The detailed characterization of the damage structure will be published in a future article.

2. Ion beam generation and conduction to the sample position

The ion beams used for radiation damage studies at DCF are produced using a 5 MV tandem Pelletron ion accelerator, in combination with the following negative ion sources: (1) a Source of Negative Ions by Caesium Sputtering (SNICS source) that produces heavy ion beams with a current of $\approx 10\,\mu A$ by bombarding the selected cathode material with Cs^+ ions [17,18]; (2) a TORoidal Volume Ion Source, i.e. TORVIS, where gas (H or He) is ionised by the plasma produced by a tungsten filament [19]. Due to the low electron affinity of helium, He^+ ions are first produced in the TORVIS source, and then passed through a Rubidium charge exchange cell to produce He^-/He^{2-} ions [20]. The TORVIS source is capable of delivering negative ion beam currents up to 100 μA (H) or 15 μA (He). The ion beam is extracted from the operative source, pre-accelerated, analysed by the injection magnet, and then accelerated by the terminal potential of the Pelletron. The negative ions pass through Ar stripper gas that converts them into positive ions. The energy of the ion beam exiting the Pelletron tank corresponds to:

$$E = (q+1) \times V_{term} + E_{inj} \quad (1)$$

where q is the charge state of the ions leaving the gas stripper, V_{term} is the applied terminal voltage and E_{inj} the injector energy, generally being of the order of a few tens of keV. The beam currents and energies achievable using this accelerator system are compared to those reported for other ion irradiations facilities in Table 1. For instance, proton beams of up to 10 MeV in energy are available using our accelerator system. These ions will have a penetration depth of $\approx 260\,\mu m$ in 20/25 stainless steel, which makes macro-scale testing of the irradiated materials feasible.

The positive ion beam generated is further directed into the beamline, at the end of which we are performing the radiation damage studies of nuclear materials. For this purpose we make use of a switching magnet with a length of $R_P = 0.48$ m. By using the expression:

$$R = \frac{R_P}{2 \times \sin\left(\frac{\phi}{2}\right)} \quad (2)$$

and the values of R_P and the deflecting angle (e.g. $\phi = 30^\circ$), we obtain a value of 0.93 m for the radius of curvature, R, of the trajectory of the ions to be injected into the 30° beam line. The applied field (B) in the switching magnet allows us to select the desired charge state of the ions that will be injected into the beamline, according to:

$$B = \frac{1440}{R}\sqrt{\frac{m \times E}{q^2}} \quad (3)$$

where m denotes the mass of the ions. The maximum field is 2×10^4 T; this constrains the energy, E, charge state, q, and mass of ions, m, available in the beam lines.

Fig. 1 displays the principal components of the beamline developed for radiation damage of materials for nuclear reactor applications. After being deflected by the switching magnet, the intensity of the beam can be measured by a Faraday cup. A rotating wire beam profile monitor (BPM) is then used to observe the beam profile. A quadrupole magnet is then used to re-focus the beam to a size of approximately 4–5 mm at the sample position.

3. Beam profile at the sample position

The beam profile at the end of the line is observed using a quartz scintillator slide before the sample position. Additionally, we achieved a uniform irradiation of a total sample area of 0.5–6 cm^2 by using a beam scanner in combination with a set of four independent slits, both installed between the quadrupole magnet and the sample position.

Table 1
Experimental capabilities of selected ion accelerator facilities used for radiation damage studies of nuclear materials [32–36]. p- protons, HI- heavy ions. Values in brackets are for accelerator to be installed by September 2015.

Facility	Primary beam	Dual Beam	Triple beam	Thermal control (°C)
Dalton Cumbrian Facility (DCF)	*p* 10 MeV 100 μA He 15 MeV 15 μA HI 10 μA	(*p* 3 MeV)		ambient – 400
Michigan Ion Beam Laboratory (MIBL)	*p* 3.2 MeV 70 μA			−180–600
JANNUS Saclay	HI 3 MV $<100\,\mu A$	HI 2 MV $<100\,\mu A$	p,d, ^{3}He, ^{4}He 2.5 MeV 40 μA	−195–850
Helmholtz Zentrum Dresden Rossendorf (HZDR)	p 6 MeV 0.5 μA	HI 450 keV 1 μA		ambient – 600
DUeT /HiMAS Kyoto University	HI e.g. Si 6.8 MeV 100 μA	He 1 MeV 100 μA	HI e.g. Ar 5 keV 40 μA	−270 – 1500
Paul-Scherrer-Institute (PSI)	p 72 MeV 50 μA			

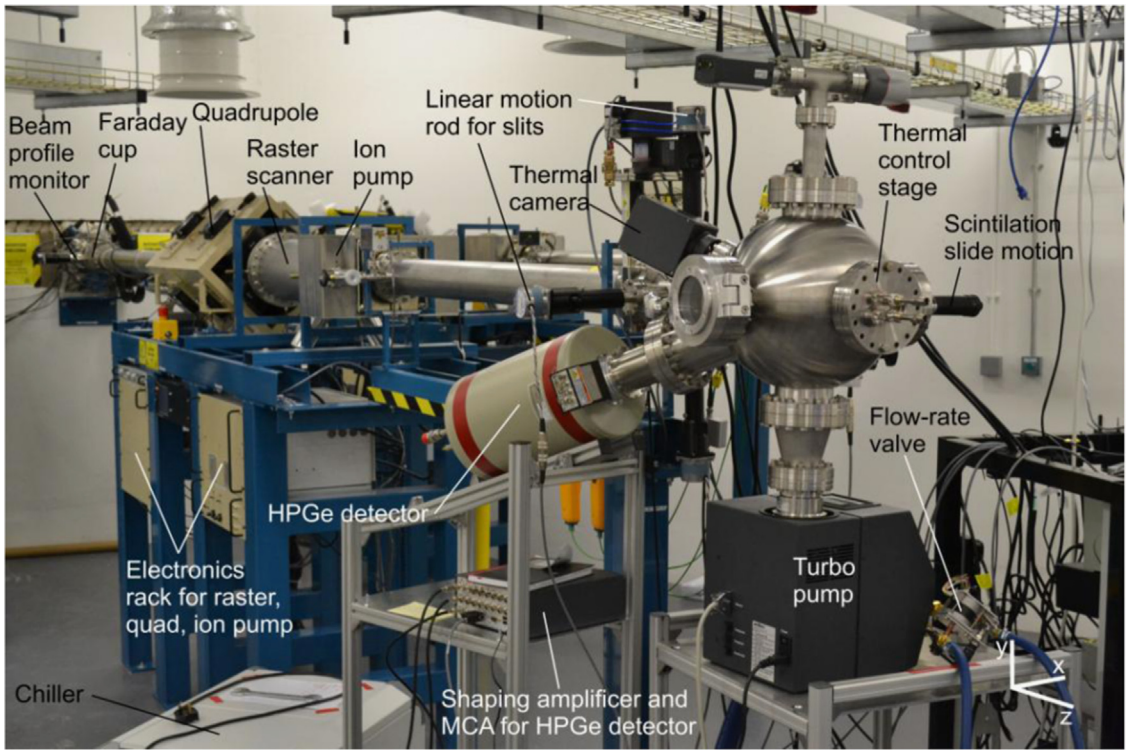

Fig. 1. Principal components of the beam line developed at the Dalton Cumbrian Facility for accelerated studies of radiation damage effects in nuclear reactor materials.

3.1. Slits

The slits system consists of four independent tantalum vanes mounted using ceramic bolts and washers on linear manipulation rods, as shown in Fig. 2a. The linear motion of the rods is driven by stepper motors. This allows the position of the vanes to be adjusted remotely. Four coaxial feedthrough connections and four thermocouple feedthroughs are built into the slits chamber. The vanes are electrically isolated from the chamber, and are connected via the coaxial feedthroughs to picoammeters, allowing the beam current on each vane to be measured simultaneously. The optimisation procedure of beam position aims to yield equivalent

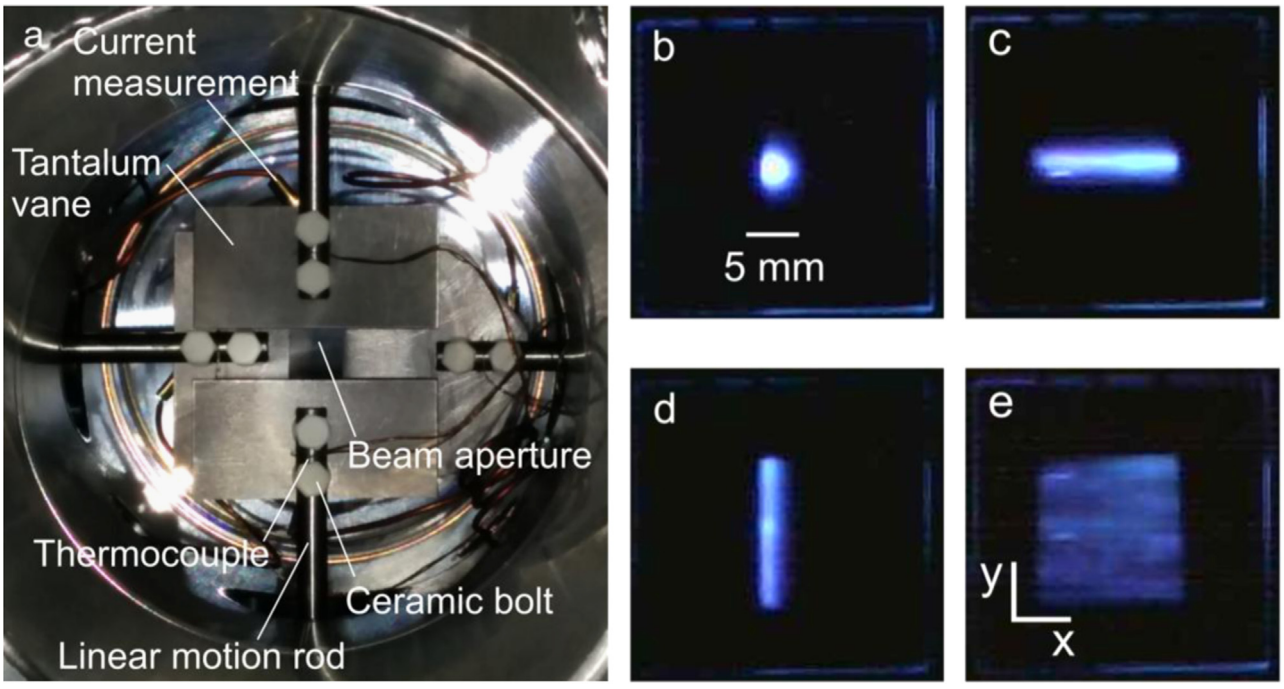

Fig. 2. (a) Slits system used to optimise the beam position on the sample, and to define the area of the sample to be irradiated uniformly by the ion beam; silica slide positioned in front of the sample and viewed by a visible-light webcam installed in a 30° viewport of the vacuum chamber with (b) the scanning system off, (c) the beam scanned in the *x*-direction, (d) the beam scanned in the *y*-direction and (e) the beam scanned in both *x*- and *y*-directions.

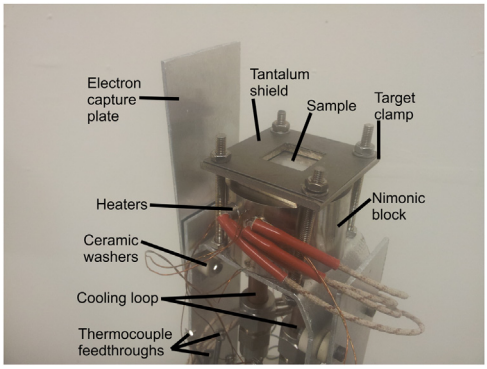

Fig. 3. Sample stage designed to perform accelerated irradiation experiments up to 400°C using ion beams under controlled conditions of temperature and dose.

current readings in the four vanes. A total beam power in the 1 kW range is possible, and roughly 1/3 of that power will be deposited on the slits. Thermocouples spot-welded to the steel rods supporting the vanes are used to monitor the thermal load caused by the ion beam.

3.2. Beam scanner

The scanning system is located between the quadrupole magnet and the slit system. The scanner applies triangle-wave electric potentials perpendicular to the beam direction. The scanning frequencies in the *x*- and *y*-directions are manufacturer-locked at the values of 517 and 64 Hz, and the scanning potential may be altered up to a maximum of 10 kV in order to adjust the scanning area on the sample. The maximum deflection angle of the beam with respect its reference positon along the travelling direction is $\pm 3°$. In order to achieve a sharp edge on the scanned beam profile, the beam is over-scanned by its full width onto the vanes of the slits system.

3.3. Scintillation slide

At the start of the irradiation experiment, a silica slide is positioned in front of the sample using a linear manipulation rod. The silica scintillates under irradiation, and the scintillation is observed using a visible-light webcam installed in a 30° viewport. The scintillation of the slide under various scanning conditions is shown in Fig. 2b–e. In 2b, the non-scanned Gaussian beam distribution is observed on both axes, while in Fig. 2c and d and e, the beam is over-scanned onto the slits in the *x*-, *y*- and both axes, respectively. The scintillation brightness shows a hard edge, since the irradiated area is defined by the position of the slits system in both directions.

4. Description of the sample stage

The sample stage for these irradiation experiments is shown in Fig. 3. Flat polished samples with dimensions of 50×30 mm^2 are mounted on a NIMONIC75® alloy block [21]. A pair of heaters is mounted on the block close to the sample. Good thermal contact between the Nimonic block and the sample is obtained at high temperatures by placing a shim containing low-melting point metal such as indium (156 °C) in between sample and block. The sample covers completely the indium film, and the whole assembly is held in place by a metallic window, covered by a tantalum shield to protect target station components from potential beam misalignments. A second layer of indium metal contact and an auxiliary heater can be added, so that the whole assembly ordered as follows: Nimonic block, indium film, auxiliary heater, indium film, metallic window and the tantalum shield facing the incoming beam.

During the experiment, the sample temperature is regulated via (1) the power input in the heaters and (2) the flow of water in the cooling loop, which passes through the Nimonic block and leads towards a water chiller. A thermal gradient is established across the block, allowing the sample temperature to be increased while maintaining relatively low temperatures in the cooling loop. Temperature monitoring is performed using K-type thermocouples welded in the sample surface close to the irradiated area, and also via a pyrometer that collects 2D images of the irradiated sample surface. The stage is mounted on a vacuum flange which provides feedthroughs for heater power, beam current measurement, coolant flow and five K-type thermocouples. An additional plate is installed parallel to the stage to collect the potential secondary electrons emitted during the sample bombardment with the ion beam.

A bespoke vacuum chamber has been commissioned for the end station of the beam line, as can be seen in Fig. 1. The chamber consists of a 300 mm diameter spherical body with six DN100CF flanges at 90° to one another. Additionally, there are three DN40CF and one DN100CF flange at 30° with respect to the beam direction. Three of these additional flanges are devoted to the pyrometer, the visible light camera and the gamma spectrometer. The sample stage is installed in one of the 90° DN100CF flanges, with the sample surface facing the incoming beam. The stage is electrically isolated from the rest of the vacuum system to allow for continuous current monitoring during irradiation.

The sample stage and the ancillary instrumentation are connected to the data acquisition system, which records the following data every 2.2 s: (1) the irradiation time in ms; (2) the integrated charge deposited on the stage, (3) the current on each of the vanes of the slits systems and on the secondary electron plate; (4) up to five thermocouple measurements, (5) the mean value, the standard deviation and the variance of the temperature on selected area(s) of the IR image; (6) the valve position that controls the flow rate of the cooling loop, and the temperature of the water entering the cooling loop; (7) the power applied to each of the heaters, and (8) the pressure level in the chamber.

5. Measurement of the irradiation temperature

5.1. Preliminary heat flow simulations

During the design of the sample stage, we performed heat flow simulations using the ANSYS Fluent 14.5 finite element computational modelling software. The simulations modelled the thermal energy transfer, black body radiation using discrete ordinates, and viscous flow using standard k–ε mode [22]. We used a simplified description of the sample stage consisting of a $1 \times 20 \times 20$ mm^3 aluminium target, a 1 mm-thick layer of liquid indium thermal contact, the Nimonic block and the water in the cooling loop. We used the values of 8370 kg/m^3 (Nimonic) and 7310 kg/m^3 (indium) for the density, 461 J/kg/K (Nimonic) and 254 J/kg/K (indium) for the specific heat, and 11.7 W/m/K (Nimonic) and 83.7 W/m/K (indium) for the thermal conductivity, and 0.0012 kg/m/s (indium) for the viscosity [21,23]. All other materials used default values. The heaters and the beam heating process were modelled as heat flows across the appropriate boundaries, and the water flow was defined as a mass-flow inlet and a pressure outlet at the ends of the water loop. The modelled thermal inputs/outputs were the heaters, beam heating, water flow and black body radiation.

Fig. 4a and b displays an illustrative example of the temperature profile along two plane views derived from these simulations,

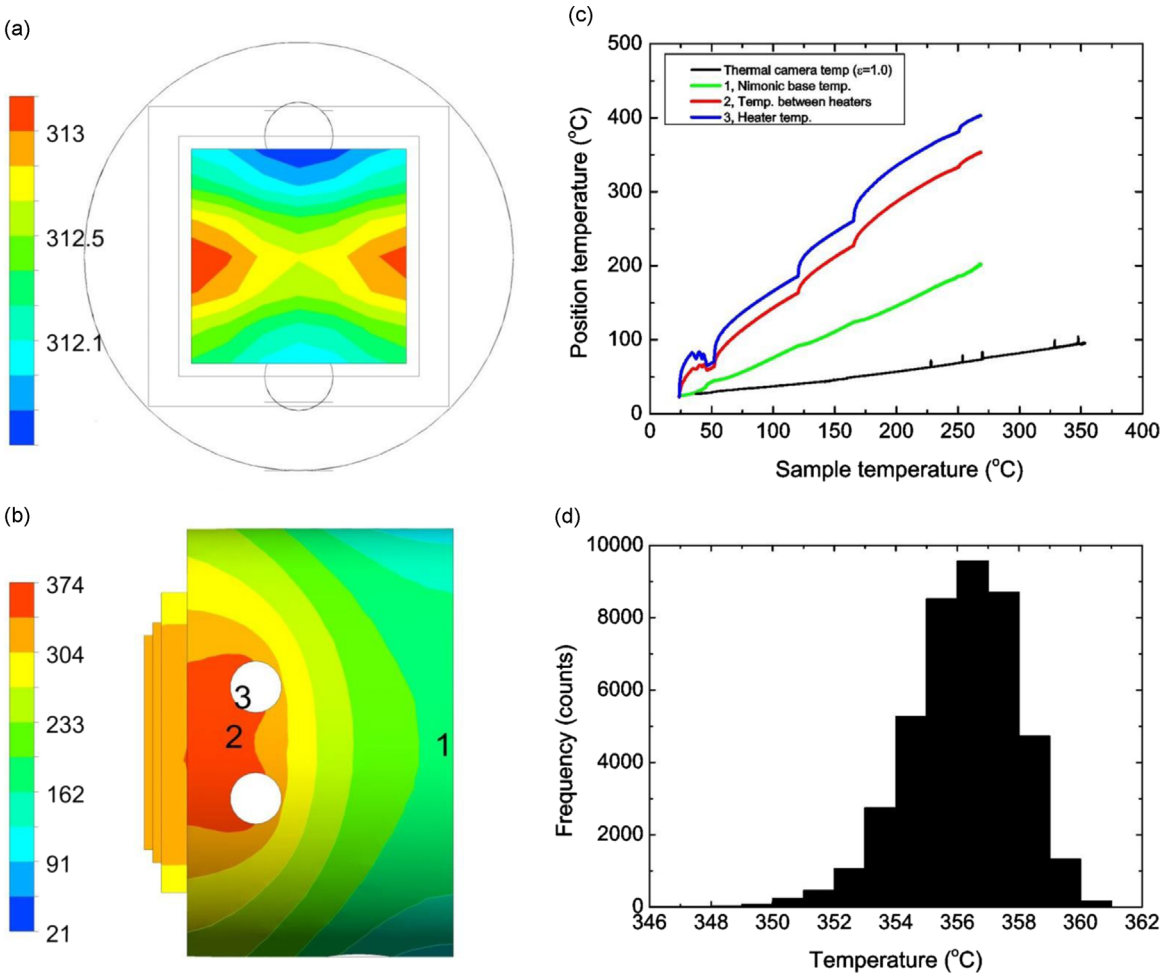

Fig. 4. Simulated temperature profile (a) of the sample surface and (b) through the Nimonic block; (c) variation of the sample temperature measured using the pyrometer, and also on three different locations on the sample stage (labelled 1–3 in (c)), with the sample temperature measured using thermocouples spot welded on its surface; (d) distribution of emissivity-corrected temperature values measured during continuous proton irradiation using the pyrometer.

using 150 W power on each heater, no additional heating from the beam, and a water flow rate of 1 l/min. The heaters were assumed to transfer their maximum power to the Nimonic. Modelling solid-to solid thermal contact is difficult, especially in this case where the contact takes place in ultra-high vacuum. Poor thermal contact would have resulted in the heaters being much hotter than the Nimonic block, and it would have been impossible to run them at their full power without overheating. This was overcome by the introduction of Ga–In–Sn eutectic between the heaters and the block. The results of the simulations revealed that the temperature gradient across the sample is minimal (± 0.5 at 312 °C). The temperature takes its maximum value between the heaters, with the sample slightly cooler and a sharp thermal gradient of ~180 °C between the hottest point and the base of the block. The simulations also showed that without beam heating, it is possible to heat the sample to 440 °C by using the maximum power of 180 W on each heater and a water flow rate of 0.12 l/m.

5.2. Temperature mapping during irradiation

We have mapped the sample temperature during heating/ion irradiation using a pyrometer installed at 30° viewport of the vacuum chamber. The pyrometer used in this experiment offers a pixel size of 0.25 mm at the sample, which would allow measurements of 2 mm matchstick samples without having edge effects. The pyrometer measures the black body temperature, which is related to the temperature of the sample by its thermal emissivity. The emissivity of metals is strongly dependent on material type, surface roughness and temperature. Samples used in ion irradiations must be highly polished so that surface roughness is minimised as compared to the penetration depth of the ion beam. Consequently, the emissivity of each sample must be calibrated independently at the temperatures relevant to the irradiation experiment. Before switching on the beam, the sample is heated to the relevant temperature range to determine the values of the sample emissivity as a function of temperature. This is achieved by normalising temperature measured without beam using the pyrometer to the value obtained from a set of thermocouples spot welded on the sample surface. Once the irradiation has finalised, the sample emissivity is measured again at the same temperature to ensure that its value has not changed during the experiment.

Fig. 4c shows the experimental values of the sample temperature measured using the pyrometer before the emissivity correction, and also on three representative locations on the sample stage, as a function of the sample temperature measured using thermocouples spot welded on its surface. The power to the heaters was changed during this process, giving rise to the wave-like deviations from the linear trend. Fig. 4d displays the histogram of sample temperature values after taking into account the temperature-dependent sample emissivity. A sample temperature of 356(2) °C with a total range of 348–361 °C has been measured over a 24 h period of continuous proton irradiation of the 20/25 stainless steel sample. This temperature variation is deemed

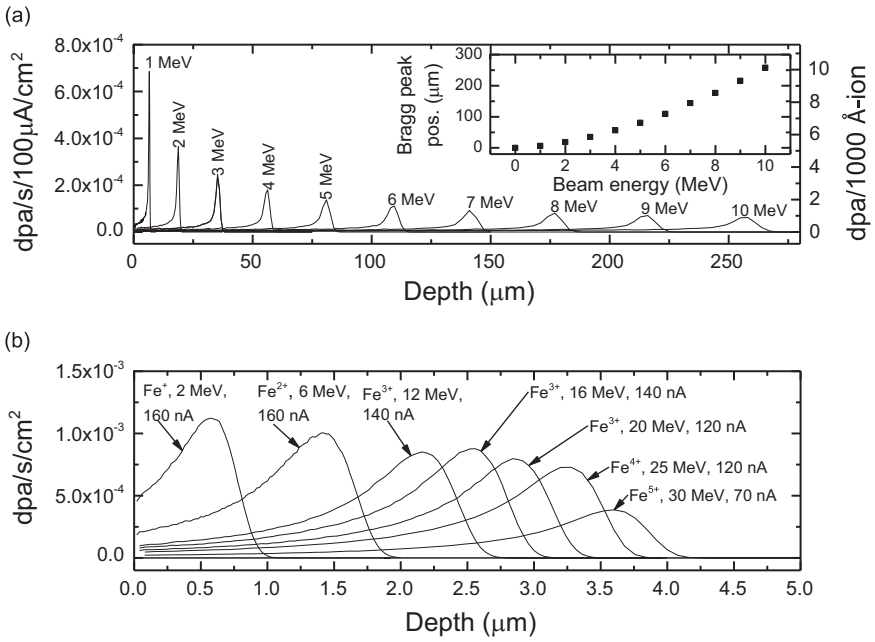

Fig. 5. Calculated damage profiles in 20/25 stainless steel using the SRIM code, in the case of (a) protons at selected energies up to 10 MeV. The inset corresponds to the Bragg peak position with respect to the sample surface as a function of beam energy; (b) iron ions at selected charge states, energies and beam currents.

Table 2
Potential nuclear reactions taking place during proton irradiation of 20/25 stainless steel using a beam energy of 3 MeV.

Target isotope fraction in 20/25 steel (atomic %)	Energetically possible reactions leading to active products	Literature values for reaction probability at 3 MeV nuclei/ incident proton or barns (b)	$T_{1/2}$ product	Energy (keV)	Intensity (%)	Energy (keV)	Intensity (%)	Energy (keV)	Intensity (%)
0.9	$^{50}Cr(p,\gamma)^{51}Mn$	2.3×10^{-8} [37]; 144 μb [38]	46.2 m	511	194	5	1	749	0.3
18	$^{52}Cr(p,\gamma)^{53}Mn$	391 μb [39]	3.74×10^{6} y	5	22	6	2		
	$^{52}Cr(p,\alpha)^{49}V$	0 b [40]	330 d	5	19				
2	$^{53}Cr(p,\gamma)^{54}Mn$	175 μb at 2.3 MeV [41]; 127 μb [40]	312 d	835	100	5	22	6	2
	$^{53}Cr(p,n)^{53}Mn$	40 mb [42]; 50 mb [40]	3.74×10^{6} y	5	22	6	2		
0.5	$^{54}Cr(p,n)^{54}Mn$	30 mb [43]; 53 mb [44]; 29 mb [45]	312 d	835	100	5	22	6	2
16.2	$^{58}Ni(p,\alpha)^{55}Co$	90 μb at 7.4 MeV [46]; 2×10^{-17} b [40]	17.5 h	511	152	931	75	477	20
6.2	$^{60}Ni(p,\alpha)^{57}Co$	1 mb at 6.8 MeV [47]; 0.2 nb [40]	272 d	122	86	136	11	14	9
	$^{60}Ni(p,\gamma)^{61}Cu$	3.1×10^{-8} [37]; 301 μb [48]	3.33 h	511	13	284	12	656	11
0.9	^{62}Ni None								
0.7	$^{55}Mn(p,n)^{55}Fe$	45 mb [42]; 56 mb [49]	2.74 y	6	27				
1.1	$^{28}Si(p,\gamma)^{29}P$	3.9×10^{-9} [37]; 680 nb [40]	4.14 s	511	200	1273	1	2426	0.4
3.1	$^{54}Fe(p,\gamma)^{55}Co$	8.2×10^{-9}[37]; 55 μb [39]; 500 μb [50]	17.5 h	511	152	931	75	477	20
48.3	$^{56}Fe(p,\gamma)^{57}Co$	46 μb [50]	271 d	122	86	136	11	14	9
	$^{56}Fe(p,\alpha)^{53}Mn$	5×10^{-14} b [40]	3.74×10^{6} y	5	22	6	2		
1.1	$^{57}Fe(p,\gamma)^{58}Co$	63 mb [40]	70.9 d	811	99	511	30	6	23
	$^{57}Fe(p,\gamma)^{58}Co^{*}$	940 mb [40]	9.10 h	7	24	8	3	25	0.04
	$^{57}Fe(p,\alpha)^{54}Mn$	1.4 mb at 4.8 MeV [49]; 10 nb [40]	312 d	835	100	5	22	6	2
	$^{57}Fe(p,n)^{57}Co$	17.8 mb [51]; 12.4 mb [42]	271 d	122	86	136	11	14	9

acceptable according to the ASTM Standard Practice for Neutron Radiation Damage Simulation by Charged-Particle Irradiation [15].

6. Radiation damage dose

In materials damage research, the damage of a material is described using the concept of displacements per atom (dpa). The Norgett, Robinson and Torrens (NRT) model [24,25] forms a broadly recognised standard approach to calculating this value. These calculations are conveniently performed using the Stopping and Range of Ions in Matter (SRIM) code in the 'Quick damage' model [26,27]. SRIM output has the units of 'displacements per Ångstrom-ion', which can be related to the dose rate using the following equation:

$$D = disp_{A-ion}\frac{I\times m\times 10^{8}}{A\times e\times \rho\times N_{Av}} \quad (4)$$

where D is the dose rate in units of dpa/s, I is the beam current in Amps, m is the mean mass number for the sample layer, A is the

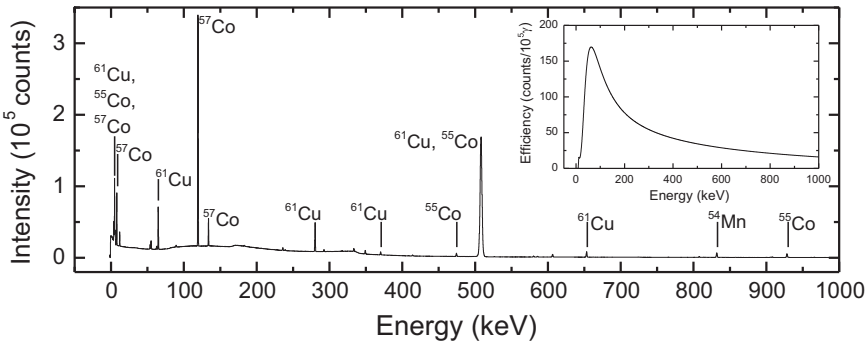

Fig. 6. Background-subtracted gamma-ray spectrum recorded during 3 MeV proton irradiation of 20/25 stainless steel. The inset corresponds to the ISOCS-calculated efficiency curve for a 1×1 cm^2 sample at 24 cm from the detector.

irradiated area in cm^2, e is the fundamental unit of charge, ρ is the mass density in g/cm^3 and N_{Av} is Avogadro's number.

The calculated damage profiles caused by bombarding 20/25 stainless steel with a proton beam at representative energies available in our facility are provided in Fig. 5a. The left-hand axis shows the maximum damage rates achievable, while the right-hand axis gives the values in the SRIM output units. The inset shows how the penetration depth, i.e. position of the Bragg peak, varies with beam energy. For damage profiles following a Bragg curve, the convention used in this paper is to define the dpa level at 60% of the Bragg peak intensity. A 3 MeV proton beam will penetrate ~40 μm in 20/25 stainless steel, while the maximum energy of 10 MeV yields a penetration depth of ~260 μm. This penetration of the proton beam allows mechanical testing of the irradiated samples to be performed [28]. Fig. 5b shows equivalent values for the damage rates achievable using Fe-ion bombardment of 20/25 stainless steel. When heavy ions are accelerated in a Tandem accelerator, the stripping process will populate a range of charge states with different intensities. The ions in higher charge states will be able to reach higher energies, according to Eq. (1). We can achieve a maximum penetration depth of ~3.7 μm when bombarding 20/25 stainless steel with Fe^{5+} ions using the maximum terminal potential of 5 MV.

The sample stage is connected to ground through an electrometer to measure accurately the charge deposited on the sample. The charge is continuously integrated in hardware during an irradiation experiment. In this way, the total measured charge will be accurate regardless of fluctuations in beam current, which would affect charge measurements made by integrating current measurements in software. Depending on the cooling fluid used, the cooling loop may provide an additional conductive path to ground. Our choice to use water as coolant turns out to alter the measured current by less than 1%. The coolant flow is seen to induce a steady current of the order of 10(5) nA on the stage when the beam is off. This background current is recorded before and after irradiation and subtracted from the measured incident charge during the irradiation. The secondary electron current consists of electrons which are displaced by ions incident on the sample. These electrons would contribute to the measured charge on the sample, but do not represent damage events. This current is measured by putting the electron capture plate at a relative positive potential and monitoring the current flow. By following these steps, we have a reliable procedure to determine the total charged being deposited on the sample during an irradiation experiment.

7. Gamma spectrometry

High-current beams of energetic protons incident on many structural materials can potentially cause activation. Simulations of stainless steel activation following 10 MeV proton irradiations for 100 h at 100 μA give an initial dose rate at 1 m of 6.3 mSv/h, falling to 0.58 mSv/h after 1000 h (i.e. 41 days) of decay. This set of simulations ignored reactions other than (p,n) and (p,γ). The major activation pathways possible at 3 MeV are presented in Table 2. In order to monitor the potential sample activation from outside the experimental hall, we mounted a Hyper-pure Germanium (HPGe) spectrometer in one of the 30° viewports of the vacuum chamber, facing the irradiated sample surface. The detector is both sensitive and discriminating, allowing gamma-emitting products to be identified well below the allowed dose rate limits. Fig. 6 shows the gamma spectrum obtained during 3 MeV proton irradiation of 20/25 stainless steel. Dedicated software is used to calculate the detector's absolute efficiency based on a geometrical model [29]. The efficiency curve given by this model for the geometry used is shown in the inset of Fig. 6. This allows the isotope activity to be calculated, from which the dose rate may be derived. The intensity of a particular peak is related to the isotope activity by the equation:

$$A = \frac{C \times I}{t \times \mathrm{Eff}(E)} \tag{5}$$

where A is the isotope activity, C is the number of counts in a peak, I is the gamma-ray intensity (i.e. the fraction of decays which give rise to this particular gamma ray), t is the measuring time of the detector (i.e. live time), and Eff(E) is the detector efficiency at energy E. The activity of the sample can be used as a control for radiation safety. The absorbed dose rate in a specific material from a particular gamma ray at a distance r from a point source is related to the activity of the isotope which gives rise to it by the equation:

$$D = \frac{A \times I}{4 \times \pi \times r^2} \frac{\mu_{en}}{\rho} \tag{6}$$

where D is dose rate and $\frac{\mu_{en}}{\rho}$ is the material-dependent mass energy absorption coefficient, obtained from tabulated data [30]. The summation must be performed across all significant peaks to yield the total dose rate. Additionally, the Excel2Genie software [31] is capable of automatically recording a series of spectra over set time-periods. This can be used to give good estimates of the decay rates for individual gamma-ray peaks, which is useful for both identifying the isotope and estimating when the dose rate will drop below the allowed limits.

Of the radioactive products in 20/25 stainless steel, both ^{61}Cu and ^{55,57}Co give rise to multiple peaks in the gamma spectrum. After correcting for the detector efficiency and the decay intensity, the measured peaks yield estimates of the isotope activity. Those estimates turn out to be within experimental error. There are some exceptions amongst low-energy peaks, where the energy calibration is less good and consequently the ISOCS efficiency calibration is less effective, and also the 511 keV peak which has multiple isotope contributions. As there is only one energetically allowed reaction path leading to ^{61}Cu, one may correct for the isotopic abundance of ^{60}Ni in the alloy (6.06%) in order to obtain a thick target yield value for the ^{60}Ni(p,γ)^{61}Cu reaction with 3 MeV protons. This value amounts to of $6.3(3)\times10^{-8}$ nuclei/incident proton, which is within an order of magnitude of an existing literature value of 2.79×10^{-8} nuclei/incident proton at 2.906 MeV [30].

8. Conclusions

We have developed a new experimental facility to perform accelerated radiation damage studies of nuclear reactor materials, by using intense proton and heavy ion beams produced by a 5 MV tandem accelerator connected to two dedicated ion sources. We have built and commissioned a dedicated sample stage that allows us to monitor in-situ the sample temperature, current on the sample, and potential activation effects via emission of gamma rays. The experimental capabilities of the beam line have been tested during a 3 MeV proton irradiation experiment on 20/25 stainless steel, currently used in AGR fuel claddings, up to a dose level of 3 dpa. The possibility of increasing the energy of the proton beam to 10 MeV opens the door to macroscopic mechanical testing of irradiated samples, and may therefore serve as a basis for simulating and predicting potential losses of structural integrity in neutron-irradiated reactor materials and components. Future efforts will focus on performing heavy ion irradiations to reach higher radiation dose levels, and also to adapt the sample stage to be inserted into a hot cell, aimed to perform experiments where the sample activation may go beyond allowed radiation limits.

Acknowledgements

This research was supported by The Engineering and Physical Sciences Research Council (Grants EP/K034650/1 and EP/L025981/1) and the Nuclear Decommissioning Authority through its Direct Research Portfolio and through the Dalton Cumbrian Facility Project, a joint initiative with The University of Manchester.

References

[1] J.G. Marques, Energy Conversion and Management 51 (2010) 1774.
[2] S.J. Zinkle, G.S. Was, Acta Materialia 61 (2013) 735.
[3] P. Yvon, F. Carré, Journal of Nuclear Materials 385 (2009) 217.
[4] V. Barabash, A. Peacock, S. Fabritsiev, G. Kalinin, S. Zinkle, A. Rowcliffe, et al., Journal of Nuclear Materials 367-370 (2007) 21.
[5] M. Song, Y.D. Wu, D. Chen, X.M. Wang, C. Sun, K.Y. Yu, et al., Acta Materialia 74 (2014) 285.
[6] X. Wang, A.M. Monterrosa, F. Zhang, H. Huang, Q. Yan, Z. Jiao, et al., Journal of Nuclear Materials 462 (2015) 119.
[7] M.B. Toloczko, F.A. Garner, V.N. Voyevodin, V.V. Bryk, O.V. Borodin, V.V. Mel'nychenko, et al., Journal of Nuclear Materials 453 (2014) 323.
[8] W. Hoffelner, Journal of Nuclear Materials 409 (2011) 112.
[9] M. Samaras, M. Victoria, W. Hoffelner, Nuclear Engineering and Technology 41 (2009) 1.
[10] R.S. Nelson, D.J. Mazey, J.A. Hudson., Journal of Nuclear Materials 37 (1970) 1.
[11] G.L. Kulcinski, A.B. Wittkower, G. Ryding., Nuclear Instruments and Methods 94 (1971) 365.
[12] G. Was, Journal of Materials Research 30 (2015) 1158.
[13] G. Was, Z. Jiao, E. Getto, K. Sun, A.M. Monterrosa, S.A. Maloy, et al., Scripta Materialia 88 (2014) 33.
[14] G. Was, J. Busby, T. Allen, E. Kenik, A. Jenssen, S. Bruemmer, et al., Journal of Nuclear Materials 300 (2002) 198.
[15] Standard Practice for Neutron Radiation Damage Simulation by Charged-Particle Irradiation (Designation E 521-96), Annual Book of ASTM Standards, vol. 12.02, American Society for Testing and Materials, Philadelphia, PA, USA, 2004, pp. 141–160.
[16] D.J. Powell, R. Pilkington, D.A. Miller, Acta Metallurgica 36 (1988) 713.
[17] R. Middleton, Nuclear Instruments and Methods 122 (1978) 35.
[18] G.T. Caskey, R.A. Douglas, H.T. Richards, H.V. Smith, Nuclear Instruments and Methods 157 (1978) 1.
[19] K. Prelec, J.G. Alessi, Review of Scientific Instruments 61 (1990) 415.
[20] T.M. Hauser, R.E. Daniel, G.A. Norton, J.B. Schroeder, Nuclear Instruments and Methods B 249 (2006) 932.
[21] Publication Number SMC-058 Copyright © Special Metals Corporation, 2004 (Sept 04).
[22] B. Launder, D. Spalding, Computer Methods in Applied Mechanics and Engineering 3 (1974) 269.
[23] David R. (Ed.), CRC Handbook of Chemistry and Physics, 90th ed.,CRC Press, 2009–2010.
[24] M.T. Robinson, I.M. Torrens, Physical Review B 9 (1974) 5008.
[25] M.J. Norgett, M.T. Robinson, I.T. Torrens, Nuclear Engineering and Design 33 (1974) 50.
[26] J.F. Ziegler, M. Ziegler, J. Biersack, Nuclear Instruments and Methods in Physics Research Section B 268 (2010) 1818.
[27] R. Stoller, M. Toloczko, G. Was, A. Certain, S. Dwaraknath, F. Garner, Nuclear Instruments and Methods in Physics Research Section B 310 (2013) 75.
[28] G.E. Lucas, G.R. Odette, H. Matsui, A. Mösslang, P. Spätig, J. Rensman, et al., Journal of Nuclear Materials 367–370 (2007) 1549.
[29] R. Venkataraman, F. Bronson, V. Abashkevich, B. Young, M. Field, Nuclear Instruments and Methods in Physics Research Section A 422 (1999) 450.
[30] N.A. Roughton, M.J. Fritts, R.J. Peterson, C.S. Zaidins, C.J. Hansen, The online version of Atomic Data and Nuclear Data Tables 23 (1979) 177.
[31] A. Forgacs, L. Balkay, L. Tron, P. Raics, Applied Radiation and Isotopes 94 (2014) 77.
[32] D.L. Damcott, J.M. Cookson, V.H. Rotberg, G.S. Was, Nuclear Instruments and Methods in Physics Research Section B 99 (1995) 780.
[33] S. Pellegrino, P. Trocellier, S. Miro, Y. Serruys, È Bordas, H. Martin, et al., Nuclear Instruments and Methods in Physics Research Section B 273 (2012) 213.
[34] J. Kaschny, R. Kögler, H. Tyrrof, W. Bürger, F. Eichhorn, A. Mücklich, et al., Nuclear Instruments and Methods in Physics Research Section A 551 (2005) 200.
[35] A. Kohyama, Y. Katoh, K. Jimbo, Materials Transactions 45 (2004) 51.
[36] M. Olivo, E. Mariani, J. Shermana., Review of Scientific Instruments. 63 (1992) 27144.
[37] N.A. Roughton, M.J. Fritts, R.J. Peterson, C.S. Zaidins, C.J. Hansen, Astrophysical Journal 205 (1976) 302.
[38] M. Rios, B. Anderson, J. Schweitzer, Nuclear Physics A 236 (1974) 523.
[39] S. Kennett, L. Mitchell, M. Anderson, D. Sargood, Nuclear Physics A 363 (1981) 233.
[40] A. Koning, D. Rochman, Nuclear Data Sheets 113 (2012) 2841.
[41] H.J. Gardner, L.W. Mitchell, S.R. Kennett, M.R. Anderson, D.G. Sargood, Australian Journal of Physics 34 (1981) 25.
[42] C.H. Johnson, C.C. Trail, A. Galonsky, Physical Review 136 (1964) B1719.
[43] C. Johnson, A. Galonsky, C. Inskeep, Prog: Oak Ridge National Lab. Reports 2910, 1960, p. 25.
[44] S. Kailas, S.K. Gupta, M.K. Mehta, S.S. Kerekatte, L.V. Namjoshi, N.K. Ganguly, S. Chintalapudi, Physical Review C 12 (1975) 1789.
[45] J. Zyskind, J. Davidson, M. Esat, M. Shapiro, R. Spear, Nuclear Physics A 301 (1978) 179.
[46] S. Kaufman, Physical Review 117 (1960) 1532.
[47] S. Tanaka, M. Furukawa, M. Chiba, Journal of Inorganic and Nuclear Chemistry 34 (1972) 2419.
[48] C.I.W. Tingwell, V.Y. Hansper, S.G. Tims, A.F. Scott, D.G. Sargood, Nuclear Physics A480 (1988) 162.
[49] Y.P. Viyogi, P. Satyamurthy, N.K. Ganguly, S. Kailas, S. Saini, M.K. Mehta, Physical Review C 18 (1978) 1178.
[50] N. Boukharouba, C.E. Brient, S.M. Grimes, V. Mishra, R.S. Pedroni, Physical Review C 46 (1992) 2375.
[51] M. Al-Abyad, M. Comsan, S. Qaim, Applied Radiation and Isotopes 67 (2009) 122.